ELSEVIER

Journal of Structural Geology 26 (2004) 1659–1675

JOURNAL OF STRUCTURAL GEOLOGY

www.elsevier.com/locate/jsg

Comparisons between analogue and numerical models of thrust wedge development

S. Ellis[a,*], G. Schreurs[b], Marion Panien[b]

[a]*Institute of Geological and Nuclear Sciences, 69 Gracefield Rd, Lower Hutt, New Zealand*
[b]*Institute of Geological Sciences, University of Bern, Baltzerstrasse 1, CH-3012 Bern, Switzerland*

Received 6 March 2003; received in revised form 24 February 2004; accepted 25 February 2004

Available online 11 May 2004

Abstract

Analogue and finite element numerical models with frictional and viscous properties are used to model thrust wedge development. Comparison between model types yields valuable information about analogue model evolution, scaling laws and the relative strengths and limitations of the techniques. Both model types show a marked contrast in structural style between 'frictional-viscous domains' underlain by a thin viscous layer and purely 'frictional domains'. Closely spaced thrusts form a narrow and highly asymmetric fold-and-thrust belt in the frictional domain, characterized by in-sequence propagation of forward thrusts. In contrast, the frictional-viscous domain shows a wide and low taper wedge and a thrust belt with a more symmetrical vergence, with both forward and back thrusts. The frictional-viscous domain numerical models show that the viscous layer initially simple shears as deformation propagates along it, while localized deformation resulting in the formation of a pop-up structure occurs in the overlying frictional layers. In both domains, thrust shear zones in the numerical model are generally steeper than the equivalent faults in the analogue model, because the finite element code uses a non-associated plasticity flow law. Nevertheless, the qualitative agreement between analogue and numerical models is encouraging. It shows that the continuum approximation used in numerical models can be used to model frictional materials, such as sand, provided caution is taken to properly scale the experiments, and some of the limitations are taken into account.

Keywords: Analogue modelling; Numerical modelling; Thrust wedges; Strain-softening; Sand; Detachment; Scaling; Frictional; Viscous

1. Introduction

Scaled analogue models have been widely used to provide insight into the mechanics of accretion and deformation of thrust wedges and accretionary complexes (Davis et al., 1983; Malavieille, 1984; Mulugeta, 1988; Colletta et al., 1991; Liu et al., 1992; Mulugeta and Koyi, 1992; Calassou et al., 1993; Lallemand et al., 1994; Philippe, 1994; Gutscher et al., 1996, 1998; Storti et al., 1997; Nieuwland et al., 2000; Schreurs et al., 2001; Costa and Vendeville, 2002; Lohrmann et al., 2003). These experiments commonly use granular materials with frictional properties such as sand, but sometimes also incorporate materials with viscous properties (e.g. silicone polymers). The advantage of analogue models is that they permit direct observations of the evolution of deformation processes (e.g. faulting sequences). Non-destructive imaging techniques even allow the visualisation of the interior of an analogue model without disturbing it and offer the opportunity for a detailed geometric and kinematic analysis of experiments involving complex three-dimensional settings (e.g. Colletta et al., 1991; Schreurs et al., 2001).

An alternative approach to studying the dynamics of accretionary and thrust wedge systems is through the use of numerical models. These forward-running experiments are conducted directly at the scale of the natural structure and can incorporate rheology that depends on rock type, temperature, and pressure (e.g. Mandl, 1988; Mäkel and Walters, 1993; Sassi et al., 1993; Willett et al., 1993; Barnichon and Charlier, 1996; Sassi and Faure, 1997; Gerbault et al., 1998; Nino et al., 1998; Upton, 1998; Vanbrabant et al., 1999; Erickson et al., 2001; Strayer et al., 2001; Huhn, 2002).

In this study we compare analogue models to equivalent large strain two-dimensional numerical models that use the continuum approximation. We choose a contractional

* Corresponding author. Tel.: +64-4570-4730; fax: +64-4570-1440.
E-mail address: s.ellis@gns.cri.nz (S. Ellis).

0191-8141/$ - see front matter © 2004 Elsevier Ltd. All rights reserved.
doi:10.1016/j.jsg.2004.02.012

setting for our comparison and use frictional and viscous materials. By making a direct model comparison, we focus on the issues of scaling, model approximations and rheological parameters. Through measurements, we constrain as much as possible the physical properties of the analogue materials and use appropriate scaling for the numerical materials. Results give a direct indication of whether numerical models correctly model behaviour of analogue materials such as sand at a continuum level, and also highlight the strengths and weaknesses of the two modelling approaches.

2. Analogue model

2.1. Analogue materials

Both viscous and frictional materials were used in the analogue model As frictional analogue materials we used dry, almost pure quartz sand and corundum sand (Table 1). The size of the quartz grains varies between 88 and 250 μm with 90% of the grains falling within the fraction 125–175 μm. The corundum sand is slightly more heterogeneous in grain size, with 70% between 88 and 125 μm, and 12% of small grains <88 μm (Table 1). The densities of sifted quartz and corundum sand are 1.56 and 1.89 g/cm^3, respectively. The mechanical properties of the granular materials were determined using a ring-shear tester (Schulze, 1994), which consists of an annular cell containing the tested material (Fig. 1). Sand was sifted from ca. 20 cm height into the ring-shear tester. A vertical load is applied through an annular lid, which is prevented from rotating by two tie rods. To shear the sample, the cell rotates and the critical shear force necessary for shearing is measured. In order to minimise error, measurements are repeated five times using different vertical loads (varying from 1 to 5 kg, in steps of 1 kg) for each tested material and

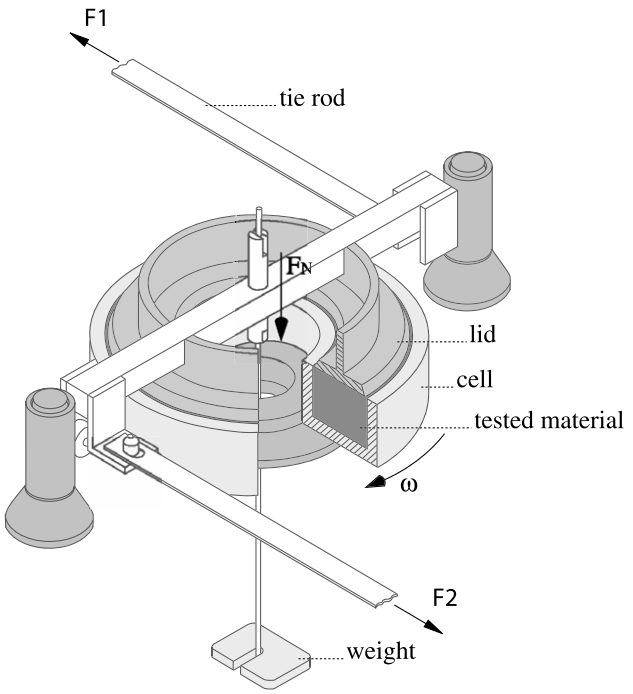

Fig. 1. Cut-away view of the ring shear test procedure. The tested material is contained in an annular cell. A vertical load (F_N) acting on the bulk solid sample is applied through an annular lid and can be adjusted with weights. Tie rods fixed to the lid prevent it from rotating. To shear the sample, the cell rotates relative to the lid with angular velocity ω (as indicated by arrow), and the shear force ($F_1 + F_2$) necessary for shearing is measured.

an experiment is repeated up to four times for each normal load. Fig. 2 shows an example of critical shear force variations with time for corundum sand using a normal load of 4 kg. An initial stage of elastic deformation is followed by a stage of plastic strain hardening that precedes the onset of failure (peak strength). Failure of the tested material corresponds to the development of narrow shear zones along which the arrangement of grains has been perturbed and dilation has occurred. Failure is followed by a stage of

Table 1
Material properties of quartz and corundum sand

	Quartz sand	Brown corundum sand
Density (sifted) in g/cm^3	1.56	1.89
Grain size	088–125 μm 5%	<0.61 μm 2%
	125–175 μm 90%	061–088 μm 10%
	175–250 μm 5%	088–125 μm 70%
		125–175 μm 18%
Composition	SiO_2 99%	Al_2O_3 95.2–95.8%
	Al_2O_3 0.4%	SiO_2 0.5–0.8%
	$Fe_2O_3 + TiO_2$ 0.05%	TiO_2 2.6%
	CaO + MgO 0.05%	Fe_2O_3 <0.2%
	K_2O/Na_2O 0.2%	CaO/MgO <0.9%
Angle of internal friction (ϕ_i)	35.5°	37.0°
Coefficient of internal friction (μ_i)	0.71	0.75
Angle of dynamic stable friction (ϕ_d)	31.2°	32.2°
Coefficient of dynamic stable friction (μ_d)	0.61	0.63
Strain-softening	15–16%	13–16%
Cohesion	2–40 Pa	29–50 Pa

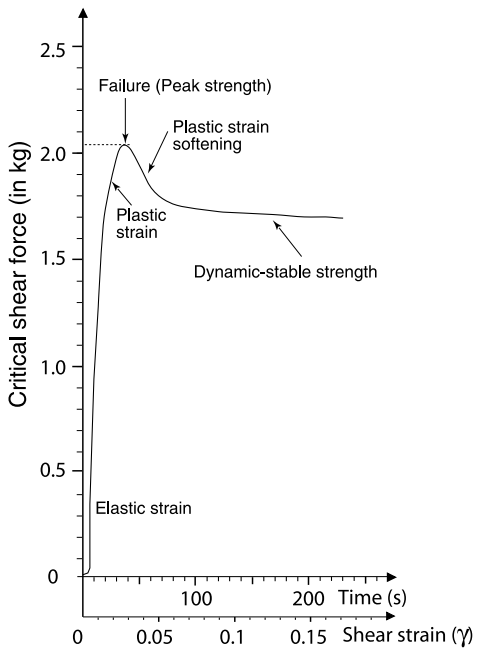

Fig. 2. Critical shear force variations recorded during a typical ring shear test of corundum sand. Applied normal load was 4 kg.

strain-softening, during which the shear force decreases until it reaches a stable value referred to as dynamic-stable strength (Lohrmann et al., 2003). The strain-softening in quartz sand and corundum sand is about 15% (difference between peak strength and dynamic-stable strength). By using the critical shear force values at peak strength and at dynamic-stable strength for different vertical loads, normal and shear stresses can be calculated and plotted against each other (Fig. 3). Linear regression analysis yields two straight lines for each tested material, corresponding to failure at peak friction and at dynamic-stable friction. From these graphs the angles of internal peak friction (ϕ_i) and dynamic-stable friction (ϕ_d) can be determined. For quartz sand they are 36 and 31°, respectively, and for corundum sand 37 and 32°, respectively. These values are similar to those determined experimentally for upper crustal rocks (Byerlee, 1978). The intersection of the failure envelope with the vertical axis (shear stress) gives the cohesion. However, data for normal stresses <500 Pa were not acquired and, hence, it becomes difficult to estimate the cohesion at very low normal stresses because of the uncertainty of extrapolations. For repeated ring-shear tests on the same material, extrapolated cohesion values vary over a wide range (peak cohesion between 2 and 40 Pa for quartz sand and between 29 and 50 Pa for corundum sand; dynamic-stable cohesion between 39 and 59 Pa for quartz sand and between 58 and 74 Pa for corundum sand). Schellart (2000) tested different granular materials and determined that at low normal stresses (below about 250–400 Pa), the fracture envelope is no longer a straight line, but shows a convex-outward shape with negligible cohesion as measured by the intercept with the axis of zero normal stress. This suggests that linearly extrapolated cohesion values at normal stresses below about 250–400 Pa are most likely overestimates.

The ring shear test results indicate that sifted dry quartz sand and corundum sand are characterised by elastic-frictional plastic behaviour with strain-hardening preceding failure at peak strength and subsequent strain-softening until a stable dynamic strength value is reached. The mechanical behaviour of quartz and corundum sand is comparable with the one exhibited by crustal rocks (Barnhoorn et al., 2004), and suggests that these granular materials are well suited to model brittle behaviour of rocks in crustal scale analogue models.

To make a comparison with numerical models, we attempted to evaluate the relationship between bulk sample strain and the strains associated with localisation of deformation in granular materials. A purely first-order analytical approach to approximate local strain values is to consider the shear deformation of an initially, close-packed arrangement of circular grains (Fig. 4). Shear deformation along a narrow fault zone involves both sideways and upwards displacement of grains, i.e. deformation occurs by

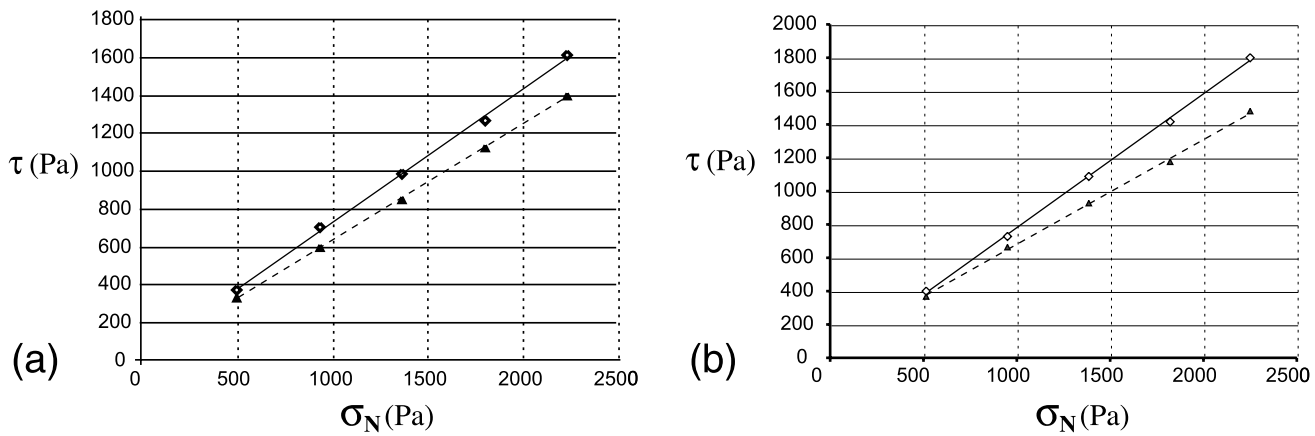

Fig. 3. Shear (τ) vs. normal (σ_N) stress for (a) quartz sand and (b) corundum sand. Internal peak friction (solid line) and dynamic stable friction (stippled line) are derived from linear regression analysis of these data. Cohesion can be inferred by extrapolation along a straight line to intersection with shear stress axis (however, see text for discussion).

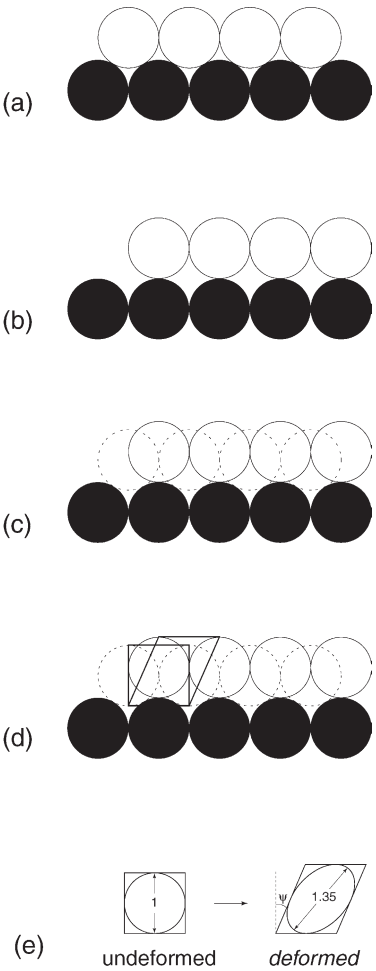

Fig. 4. Schematic illustration of shearing and dilation of perfectly spherical granular material. (a) Initial grain packing; (b) displacement of grains during shearing is accompanied by dilation; (c) comparison between undeformed and sheared configuration; (d) an initially undeformed square becomes a parallelogram during shearing and dilation; (e) the shear strain ($\gamma = \tan\psi$, where ψ is the angular shear strain) associated with the configuration shown amounts to $\tan(33°) = 0.65$; taking dilation into account gives a length increase of 35% for the principal stretching axis. Drawings based on Vermeer and de Borst (1984) and a theoretical concept developed by Chris Beaumont (pers. comm.).

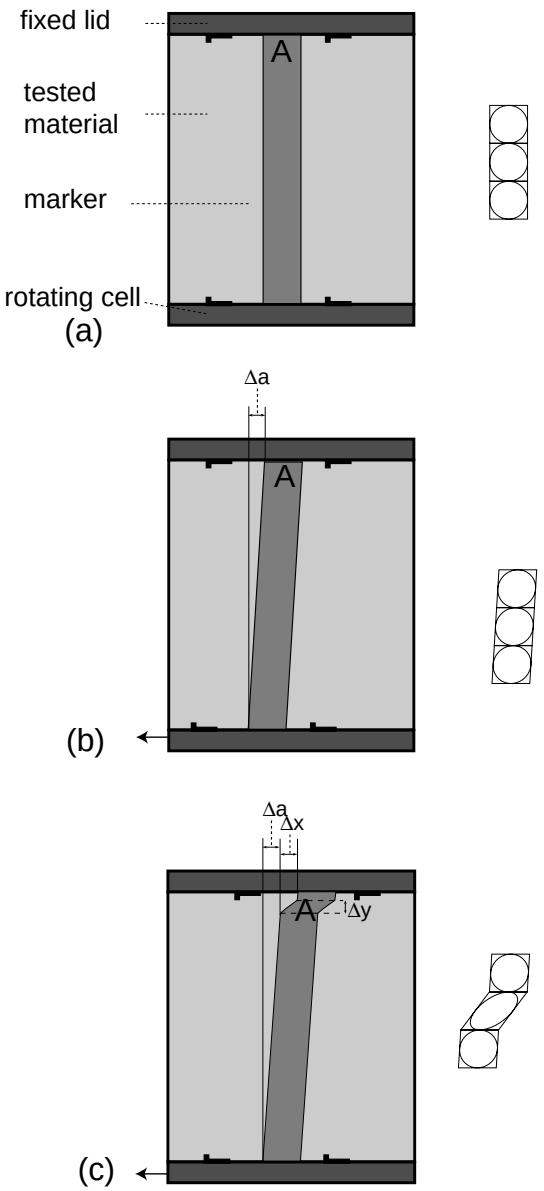

Fig. 5. Vertical sections (aligned along the ring, not radially) of the ring shear tester, (a) before rotation, (b) during elastic strain, and (c) after rotation of the cell until failure. The hypothetical marker illustrates the shearing of the bulk sample, first by elastic strain and then by plastic strain and subsequent failure at peak strength. Failure at peak strength is followed by strain-softening. Δa is relative cell displacement during elastic straining of the sand, whereas Δx is relative cell displacement during plastic straining. Δy is the shear zone width. Deformation at A is schematically illustrated by the strain ellipses next to each section. See text for discussion.

both shearing and dilation. A comparison between the undeformed stage with maximum grain contact and the deformed stage with minimum grain contact reveals that the local longitudinal strain for the principal stretching axis is about 35% (Fig. 4). The grains in our analogue models, however, are not perfectly circular but subangular and have a low sphericity. Also, the development of fault zones in the analogue model may be associated with abrasion of grains, resulting in slight grain shape changes. Therefore, the analytical approach is only considered to provide a minimum estimate for local longitudinal strain.

A second approach to estimate local strain values in narrow fault zones is to use the ring shear test results. Fig. 5 shows three hypothetical vertical sections perpendicular to the radial direction of the ring shear tester (cf. Fig. 1). The initially vertical marker tracks deformation during the ring shear experiment. The bulk sample first undergoes shearing by elastic strain, followed by plastic strain-hardening and subsequent failure at peak strength (Fig. 5). As the cell is closed during shearing, we do not know where the fault zone forms initially. Total displacement of the cell ($\Delta a + \Delta x$; see Fig. 5) at failure in different tests on quartz sand varies between 1.0 and 1.4 mm near the inner part of the cell and between 2.5 and 3.6 mm near the outer part of the cell. From computer tomography slices through our analogue models

we know that the initial fault zone width in frictional materials is about 1–1.5 mm. By taking the minimum and maximum cell displacement at which failure occurs (1 and 3.6 mm, respectively, for quartz sand) and by considering a 1-mm-wide fault zone, the local shear strain can be approximated. For quartz sand, the minimum and maximum local shear strain is 1 and 3.6, respectively. Using equations given by Ramsay and Graham (1970), the local maximum principal strain can be calculated from the local shear strain and lies between 60 and 300% for the given range of shear strain.

In the calculations above we have assumed that total cell displacement is entirely accommodated along a 1 mm narrow fault zone. Initial cell displacement, however, is taken up by elastic strain in the sand. The relative contribution of elastic strain (Δa) and plastic strain (Δx) to total cell displacement at failure can only be estimated approximately from Fig. 2 as the change from elastic to plastic strain is not sharp but transitional. If we correct for the contribution of elastic strain to cell displacement and again take a fault zone width of 1 mm, the minimum and maximum local shear strain values will be lower (0.8 and 2.5, respectively) and the local maximum principal strain ranges between 47 and 182%.

In our analogue model set-up dry quartz sand directly overlies part of the wooden base of the experimental apparatus. Therefore, we also determined the basal friction using the ring shear tester. An annular piece of wood was placed on the bottom of the cell and overlain by a layer of quartz sand. The technique to measure basal peak and dynamic stable strength is the same as described before. The angle of dynamic stable friction is 28°.

As a viscous analogue, we used a transparent silicone polymer (SGM 36, a polydimethyl-siloxane) with a Newtonian viscous behaviour. It has a density of 0.965 g/cm^3 and a linear viscosity of 5×10^4 Pa s at room temperature and at strain rates below 3×10^{-3} s^{-1} (Weijermars, 1986). Viscous polymers are considered a good analogue material for simulating viscous flow of salt/evaporites in the upper crust or rocks in the lower crust (Vendeville et al., 1987).

2.2. Analogue modelling procedure

The experimental apparatus used to model thrust belt development consists of a rectangular box with a vertical mobile wall. The base and walls of the box are composed of wood. Our experiments were designed to test the influence of mechanical layering on thrust belt development. A 5-mm-thick rectangular-shaped slab (length 40 cm, width 17 cm) of viscous silicone is placed over part of the wooden base abutting the rigid, mobile backstop (Fig. 6). The viscous layer does not extend all the way to the opposite, fixed wall, but ends 10 cm from it. Alternate layers of sand and corundum are sifted adjacent to the viscous layer and on top of it. The undeformed model is 80 cm long, 27 cm wide and its total thickness amounts to 3 cm. For ease of description, the part of the model underlain by a viscous silicone layer is referred to as the 'frictional-viscous domain', whereas the part consisting only of granular materials is referred to as the 'frictional domain'. The mobile backstop has a basal exit slot of 3 mm height, to ensure that detachment occurs within the viscous silicone layer. The model is deformed by displacing the mobile wall, driven by a motor, at a constant velocity of 4.8 cm/h.

A spiral X-ray computed tomographer (CT) was used for the analysis of the analogue model. The viscous silicone, quartz sand and corundum sand have distinct X-ray attenuation values and their boundaries can be visualised in X-ray computed tomography (CT) images. Faults in frictional materials represent zones of dilation and consequently show a difference in X-ray attenuation with respect to unfaulted domains.[1] Periodic CT acquisition allowed us to monitor the three-dimensional evolution of the model structures at successive stages of deformation. X-ray CT images were digitally enhanced using computer visualisation software. There was a marked difference in thrust belt development between the purely frictional and the frictional-viscous domains and their evolution is described separately (Sections 4.1 and 5.1, respectively) using successive transverse CT images through the progressively deformed model.

3. Numerical model

3.1. Numerical modelling procedure

The two-dimensional numerical code has been specifically designed to investigate situations with a high percentage of finite strain (Beaumont and Quinlan, 1994; Fullsack, 1995). It uses the arbitrary Lagrangian–Eulerian method to compute large deformation while avoiding numerical problems associated with extreme deformation of the grid. The code is modified from the method described in Fullsack (1995), in order to reproduce the boundary conditions shown in Fig. 7. Gravity is included in the model.

In the numerical model sand is modelled as a frictional plastic material that undergoes subsequent strain-softening and silicone as a linear viscous material (where deviatoric stress is linearly related to deviatoric strain-rate by the viscosity). Elasticity is not incorporated in the code, i.e. it is rigid-plastic in the frictional domain. The elastic modulus of the analogue materials scaled to the numerical experiment is rather high (ca. 40–60 GPa) supporting this assumption. Sensitivity tests using the Abaqus finite element engineering package, which includes elasticity but can only model small

[1] Note that dilation in sand occurs slightly before frictional failure and softening (Lohrmann et al., 2003), so that faults imaged in the sand and corundum will appear before significant strain-softening has taken place. This should be remembered when comparing with numerical experiments showing strain-softened regions in Sections 4 and 5.

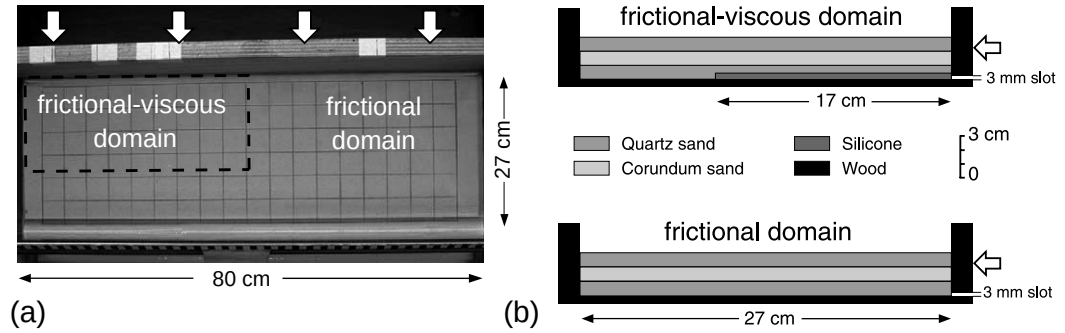

Fig. 6. Analogue experimental set-up. (a) Plan view showing variation in basal properties. (b) Cross-sections through frictional-viscous and frictional domains.

amounts of deformation (Abaqus, 2001) can be used to demonstrate that the elastic response does not significantly change results, since the material rapidly stresses to yield.

Since the code models frictional behaviour using a Coulomb yield criterion with non-associated flow law, volume changes are neglected, i.e. the angle of dilation is set to zero (Zienkiewicz et al., 1975; Willett, 1992). Consequently, the initial angle of shear zones is at 45° to the maximum compressive stress rather than $(45°-\phi_i/2)$ as predicted for associated Coulomb plasticity (Willett et al., 1993). The shear zones, however, can change their orientation during progressive deformation. We assume that first order effects of dilation on shear zone development can be represented within a bulk strain-softening parameter. Strain-softening is applied after a threshold strain is reached, as described in Section 3.3. Strain-softening results in a decrease in the internal angle of friction used in the model.

Model boundary conditions match those in the sandbox experiment as closely as possible (Fig. 7). A wall friction is applied at the wall and base of the model following a Coulomb law controlled by static-stable friction, where the shear stress for sliding is proportional to the angle of basal friction ϕ_b and the normal stresses σ_n acting on the boundary, as follows:

$$\tau = \tan(\phi_b)\sigma_n \quad (1)$$

Velocity boundary conditions are applied at a uniform rate along the right-hand wall above the slot, which has a smoothed horizontal exit velocity in order to prevent an abrupt velocity discontinuity between the wall and underlying slot material. Tests in which a more abrupt velocity discontinuity was applied yielded similar results but became unstable due to extreme shear pressures at the discontinuity. We consider the approximation used to model the slot a reasonable one, because even in the analogue model the velocity will fall off over a finite distance due to slight irregularities in the wall geometry.

The grid dimensions are sufficiently fine to capture focused shearing, but no faults are permitted. As shear zones become focused as a result of strain- and/or strain-rate softening effects, a limiting width depending on grid size is approached (cf. de Borst, 1991). Although shear zones in the numerical model are broader than those in the analogue

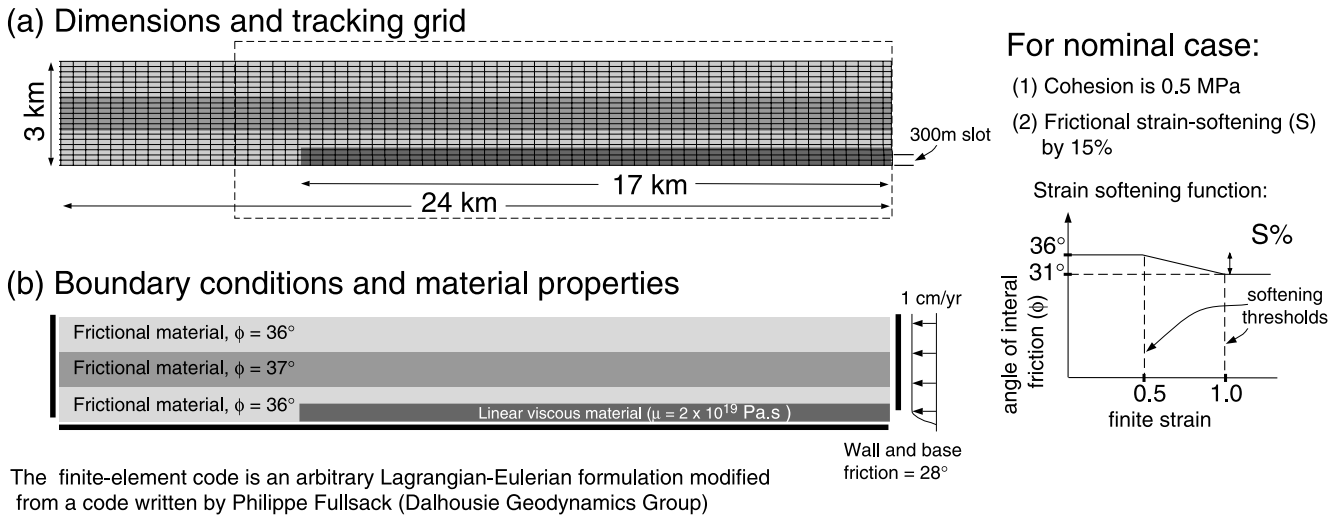

Fig. 7. Numerical model set-up. (a) Dimensions and illustration of the grid used to track finite deformation. The grid shown is a subset of the true grid resolution of the model (120 × 50 m). The dashed region outlines the part of the model domain shown in subsequent figures. (b) Boundary conditions and material properties. Bold lines show the wall and base. Panel at right shows strain-softening function used in the frictional material. Finite strain is measured as the principal stretch within each element.

model, sensitivity studies show that results for finer meshes are not significantly different (Section 6.3), and that the finite width of shear zones does not cause fundamental differences in the behaviour of the system compared with the analogue model, which can develop discontinuous faults. The element aspect ratio used in the numerical model is 2:1, below the limit at which results become significantly degraded; tests were conducted to make sure that the aspect ratio had little effect on results.

All of the numerical experiments shown here were performed at basin scale, with a model domain of 3 km depth and 24 km width, scaled up by five orders of magnitude from the analogue model. No erosion or sedimentation was applied at the free surface; however, because of the abrupt change in velocity and topography against the right hand wall, artificial damping at the surface had to be applied to prevent a 'ringing' effect against the boundary. The damping locally smoothed out ringing and tests showed that it did not significantly alter dynamics or average topography in the wall region.

3.2. Scaling considerations with the numerical model

To scale parameter values from the analogue model scale up to basin scale, we used the dynamic similarity scaling relationships discussed by Ramberg (1981) Dynamic similarity means that force ratios (compared kind-for-kind) as well as length ratios remain constant. In the case of the models investigated here, the two most important forces to be considered are F_g, the gravitational force caused by increase in potential energy of the thickened wedge; and F_v, the viscous force. These can be related by a force balance so that:

$$\frac{F_g}{F_v} = \frac{\rho g h^2}{\eta V} = \text{constant} \quad (2)$$

where h is the layer thickness, ρ is density, g is gravity, η is viscosity and V is the magnitude of velocity (Ramberg, 1981). Together with a direct relationship relating length scale of model to length scale of natural examples, this almost completely defines the scaling relationships when inertial forces may be neglected. The stresses, σ, of the frictional material may be scaled up by assuming that the depth at which cohesive strength equals lithostatic pressure remains constant to maintain dynamic similarity (Hubbert, 1937; Ramberg, 1981), so that:

$$\frac{\sigma_N}{\rho_N h_N} = \frac{\sigma_A}{\rho_A h_A} \quad (3)$$

where the subscripts N and A refer to numerical and analogue model values, respectively.

3.3. Material properties of the numerical model

In Section 2.1 we showed that parameter values for the internal angle of friction in quartz and corundum sand, densities, and viscosity of the silicone are well constrained We use the same values within the numerical model, scaled as given in Table 2. Values for cohesion and parameters controlling the strain-softening behaviour are less well constrained by the ring shear tests. Since it is not clear how to relate the bulk shear strain measurements in the ring shear tests to local strain within a finite element, the strain-softening amount and the strain-softening thresholds are also subject to uncertainty. We conduct a search around the starting values from Section 2.1 to find the best-fit model and an acceptable range for cohesion, strain-softening amount, and percentage strain at which strain-softening begins.

The strain-softening thresholds are measured with respect to the principal finite stretch within each Lagrangian element, and the internal angle of friction is decreased linearly between the two threshold values. From Fig. 2 it appears that the linear decrease in shear strength as a function of bulk strain occurs after approximately 2 × the strain needed to start softening. In the numerical model we vary the thresholds but keep the ratio between them fixed at 1:2. Strain-softening is applied as an explicit time-stepping function to avoid the bifurcation problems mentioned in de Borst (1991). Values of cohesion for a particular model run are kept constant with depth and are independent of normal stress.

4. Comparison between frictional analogue and best-fit numerical experiment

4.1. Frictional analogue experiments (Fig. 8a)

During the early stages of shortening, distributed grain flow of the frictional layers gives way to discrete faulting as the dominant mechanism of strain accommodation. A basal detachment initiates at the slot region and propagates along the base of the model. Thrust faults with opposite vergence develop (Fig. 8a: 1 cm shortening), with forward thrusts dipping more shallowly (25–28°) than backthrusts (35°). The downward converging thrust faults define a pop-up structure that roots at the base of the lowermost quartz sand layer. The forward thrust shows a slightly concave upward shape. The forward thrust is predominantly active, while

Table 2
Analogue and numerical model parameters

Scaling quantity	Analogue model	Numerical model
Length (h)	1 cm	1 km
Density (ρ)	1560 kg/m^3 (sand)	1560 kg/m^3 (sand)
	1890 kg/m^3 (corundum)	1890 kg/m^3 (corundum)
	965 kg/m^3 (silicone)	965 kg/m^3 (silicone)
Velocity (V)	4.8 cm/h	1 cm/year
Cohesion (C)	1–10 Pa	0.1–1 MPa
Viscosity (η)	5×10^4 Pa s	2×10^{19} Pa s

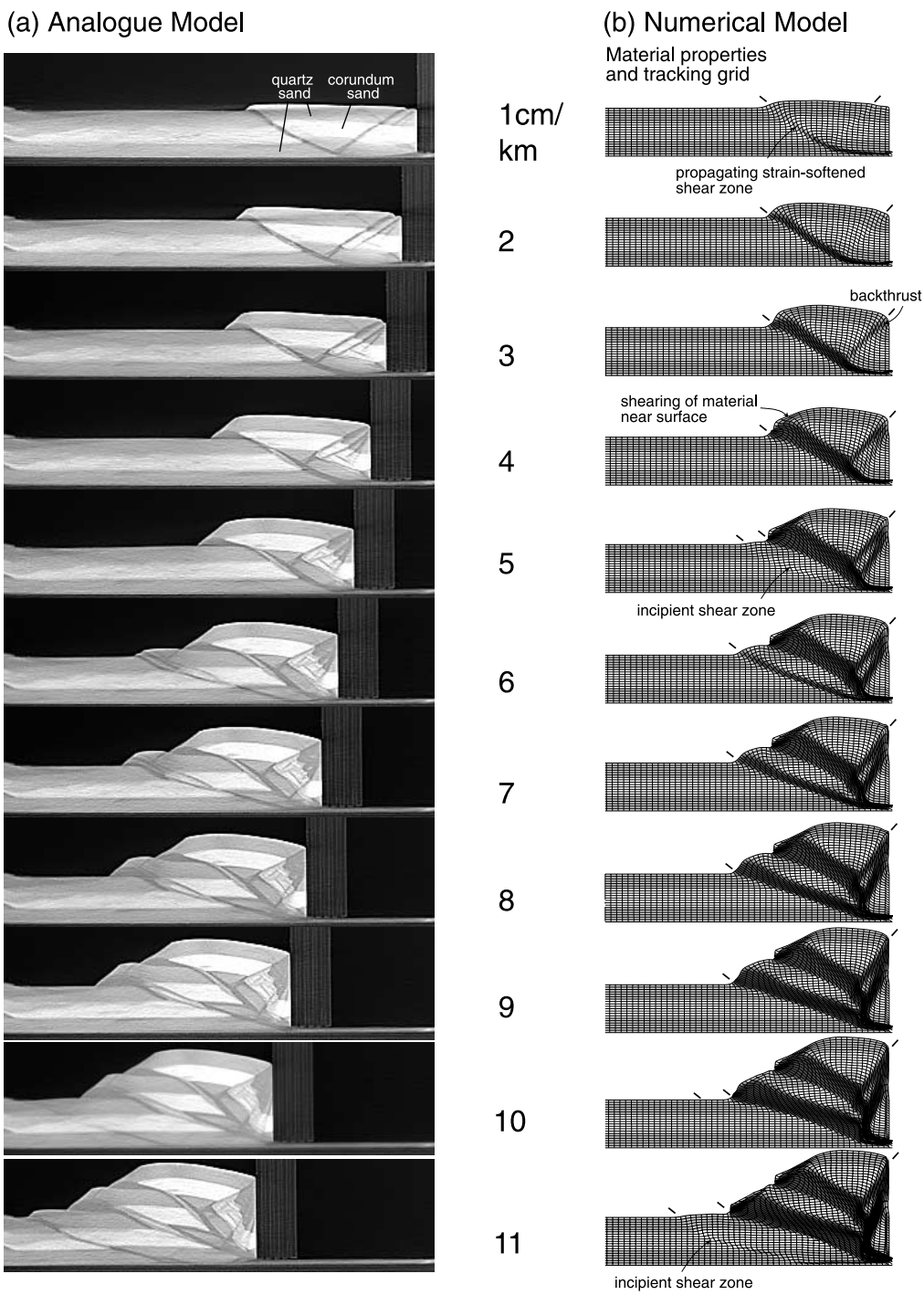

Fig. 8. (a) Results for the analogue frictional experiment. (b) Equivalent time steps for the numerical model experiment. Cohesion in the numerical model is 0.5 MPa; frictional strain-softening of 15% takes place between 0.5 and 1.0 of total strain. The small inclined lines at the top of each panel indicate actively deforming shear zones, as determined from strain-rate plots (not shown).

backthrusts form at the bend from flat to lower ramp (Fig. 8a: 2 cm shortening). Backthrusts jump episodically downward to create a series of steeply dipping thrusts that merge near the top of the model, against the backstop. The backthrusts show little movement and as they are passively transported over the forward thrust their fault dip decreases. Progressive shortening is accommodated either by diffuse deformation in the hanging wall of the forward thrust—resulting in a broadening of the zone affected by dilation—or by the development of a sub-parallel low angle thrust fault. In the latter case a small volume of frictional material completely bounded by thrust faults (i.e. a horse) is created.

With increasing deformation, the basal detachment is activated in front of the pop-up structure and a second thrust imbricate develops (Fig. 8a: 6 cm shortening). Activity along the previously formed forward thrust ceases and fault

movement is transferred to the newly developed forward thrust in its footwall. The second thrust shows a splay in its hanging wall and a horse is created. As deformation progresses, a third in-sequence imbricate thrust forms (Fig. 8a: 11 cm shortening).

4.2. Frictional numerical experiments (Fig. 8b)

As discussed above, uncertainties in cohesion and in strain-softening thresholds for the analogue materials make it difficult to merely scale up values without conducting a search in parameter space. We conducted a suite of numerical experiments with cohesion values between 0.1 and 1 MPa, and strain-softening thresholds between 0.3 and 1.0 finite strain. We found that the experiments with higher cohesion values (1 MPa) were qualitatively similar to lower cohesion experiments but that their surface slopes were too high compared with the analogue model. The most acceptable models therefore have lower cohesions (0.1–0.5 MPa, corresponding to cohesions between 1 and 5 Pa in the analogue model). Fig. 8b shows a low cohesion (0.5 MPa) numerical experiment assuming that strain-softening of the internal angle of friction by 15% takes place between 0.5 and 1.0 of total finite strain.

The dynamics of the numerical model are broadly consistent with those of the analogue experiment. An initially curved, strain-softened region develops, rooted in the slot in the right-hand wall (Fig. 8b: 1 km shortening). Because of the limited mesh resolution, the strain-softened region (which we compare with the visible faults in the analogue material) eventually broadens to a width of about 1 km, 1/3 the total layer thickness. Material between the forward thrust and the backstop is uplifted in a plug, as seen in the analogue model. The width of the plug is approximately 2 × the total thickness of the layers, somewhat less than the analogue pop-up (which has a width about 3 × the total layer thickness). Both forward and backward thrusts dip more steeply than their analogue counterparts, at 32 and 45°, respectively, and the backthrust steepens with progressive convergence rather than being rotated into a more horizontal attitude as in the analogue experiments. Wedge angles are also somewhat steeper, creating a thicker pile than for the equivalent analogue steps. We believe that these differences result from the non-associated plastic flow law, which causes thrust shear zones to form at a steeper angle. Several backthrusts develop against the wall like in the analogue model, although their spacing and time of development are somewhat different. We attribute this to the different initial fault dips and limited resolution of the numerical model.

With more convergence, the strain-softened forward thrust is displaced and uplifted towards the wall. The misalignment of this shear zone with the tip of the sheared, high stress region near the slot causes a second forward thrust to develop after a convergence of 5–6 km. Material near the first shear zone at the surface reaches the critical angle of repose and is sheared downwards. This effect is also seen in the analogue model.

After 11 km convergence a third forward shear zone develops in the numerical model, slightly later than in the equivalent analogue model. Despite the discrepancy in shear zone thicknesses and timing, the succession of forward stepping thrusts is successfully reproduced in the numerical model.

Vectors of the maximum compressive principal stress are overlain on a contour plot of log (second deviatoric strain-rate) for the frictional numerical model after 1 km convergence in Fig. 9. Maximum stresses exceeding 200 MPa are attained near the slot. This is to be expected given the very strong influence of the boundary condition in this region. Within the strain-softened shear zones, stresses are slightly reduced compared with surrounding regions, which experience stresses of ca. 100–200 MPa. These values are consistent with the range in values measured within the sandbox experiments of Nieuwland et al. (2000). They found differential stresses beneath several forward verging thrusts of ca. 2500–3000 Pa, which are equivalent to approximately 140–190 MPa at the scale of our numerical experiments. The directions and magnitudes of principal compressive stress also compare well with those predicted by the numerical models of Mäkel and Walters (1993).

Fig. 9 also shows how principal stress directions are rotated anticlockwise in low dipping shear zones. In particular, near the base of the model, the maximum principal compressive stress (σ_1) dips at about 30°. This is consistent with the sub-horizontal attitude of shear zones in this region, since slip lines in the numerical model are predicted to form at 45° to the maximum compressive stress (σ_1) (cf. $45°-\phi_i/2$ for dilational Coulomb material), The rotation of σ_1 in this region and associated development of a curved shear zone is an effect of the basal shear stress (Mandl, 1988; Mäkel and Walters, 1993).

4.3. Sensitivity analysis

One advantage of the numerical technique is that it easily allows parameter values to be varied in order to examine their influence on the solution Here, we explore the sensitivity to cohesion and the strain-softening parameters (Fig. 10).

4.3.1. Sensitivity to cohesion

Fig. 10c and d shows resultant deformation after 8 km convergence in numerical experiments in which the frictional parameters used in Section 4.2 are changed by increasing or decreasing the cohesion. The results are qualitatively similar to the frictional case in Fig. 10b, but Fig. 10c shows how a lower cohesion causes lower surface slopes to develop within the frontal thrusts. Shear zone width is also slightly reduced for lower cohesion. Increased cohesion (Fig. 10d) causes surface slopes to remain stable at

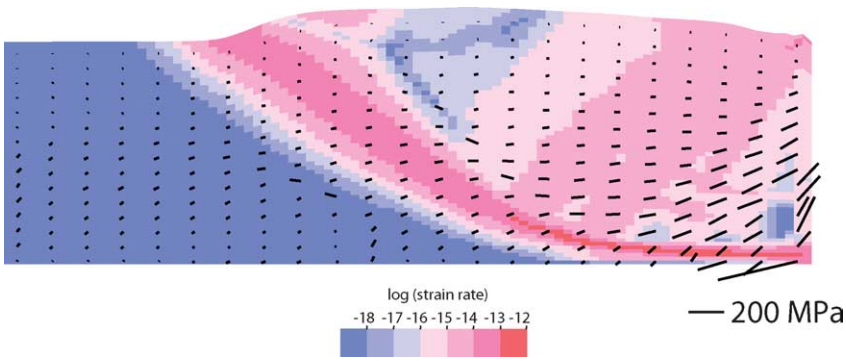

Fig. 9. Contours of log (second deviatoric strain-rate) with directions and magnitudes of principal compressive stress superimposed, for the numerical frictional experiment after 1 km convergence.

much higher values with a higher tapered wedge. The plug shows more internal deformation in this case, and formation of a third shear zone is slightly advanced.

4.3.2. Sensitivity to strain-softening threshold

As discussed in Section 2.1, the strain values at which strain-softening begins and ends are poorly known from the bulk ring shear tests. In the model shown in Fig. 10b we have assumed strain-softening begins after a finite principal stretch of 0.5 and ends at strain = 1.0. We also ran a suite of models in which the starting or ending values of sensitivity thresholds were varied, and the amount of strain over which softening occurred either kept constant or at a constant ratio of 1:2. Fig. 10e and f demonstrates that these strain-softening thresholds also produce an acceptable fit to the analogue model, although some differences are observed. For a lower strain-softening threshold (softening by 15% of original value between strain = 0.3 and 0.6; Fig. 10e) shear zone widths are increased compared with the model in Fig. 10b. Similar results were observed for a case in which strain-softening occurred from a finite principal stretch of 0.3–0.8. For higher thresholds (e.g. softening of 15% between strain = 1.0 and 2.0; Fig. 10f) the forward thrusts are narrower and there is more internal plug deformation.

4.3.3. Sensitivity to amount of strain-softening

Greater amounts of strain-softening produce slightly different dynamics in the numerical model (Fig. 10g). In this model, the extra softening causes more deformation to be partitioned onto the first forward thrust. The pop-up structure is advected over the footwall in the manner of a flat–ramp–flat before the next thrust forms. Within the plug, material is tilted backwards and only one backthrust forms. Surface slumping is more evident owing to the extreme softening in this region. The width of the forward thrust is comparable with that in the frictional model shown in Fig. 10b near the surface, but decreases with increasing depth, indicating that the down-cutting of the shear zone only takes place near the surface.

Fig. 10h shows results for a model with no strain-softening. The first thrust in this case is extremely diffuse. The marker horizon is tilted and sheared over a wide region, quite unlike behaviour of the analogue model. This model result indicates that strain-softening is not required to achieve episodic thrusting and wedge formation, but that thrusting style is much more irregular.

In summary, from sensitivity studies like those in Fig. 10 we have found that strain-softening of between 10 and 30% in the numerical experiments provides an acceptable fit. Results are not very sensitive to strain-softening threshold values, although these may control the width of shear zones that form in the numerical model, and the timing of thrust development. Higher cohesion increases taper and allows steeper surface slopes to develop.

5. Comparison between frictional-viscous analogue and numerical experiments

5.1. Frictional-viscous analogue experiment

The initial basal detachment forms within the basal silicone layer and a pop-up structure develops in the overlying frictional layers near the mobile backstop (Fig. 11a: 1 cm shortening). The forward thrust dips at 30° and the backthrust at 32°. With increasing strain both backthrust and viscous material are transported along the frontal thrust, and initiate a second back-thrust, and a splay in the forward thrust (Fig. 11a: 2 cm shortening). Movement along the forward thrust splay creates a horse that is progressively sheared as shortening progresses (Fig. 11a: 3 cm shortening). Displacement takes place dominantly along the forward thrust, and a fault-bend fold develops as material moves upward along the ramp.

As deformation progresses, a new—slightly concave upward—thrust forms far away from the mobile wall, at the foreland pinchout, i.e. at the vertical interface between basal silicone and quartz sand (Fig. 11a: 4 cm shortening). Shortening is now accommodated by coeval activity along the frontal ramp and along the forward thrust of the pop-up structure near the mobile wall. The progressive movement of the mobile wall, and the advection of silicone and

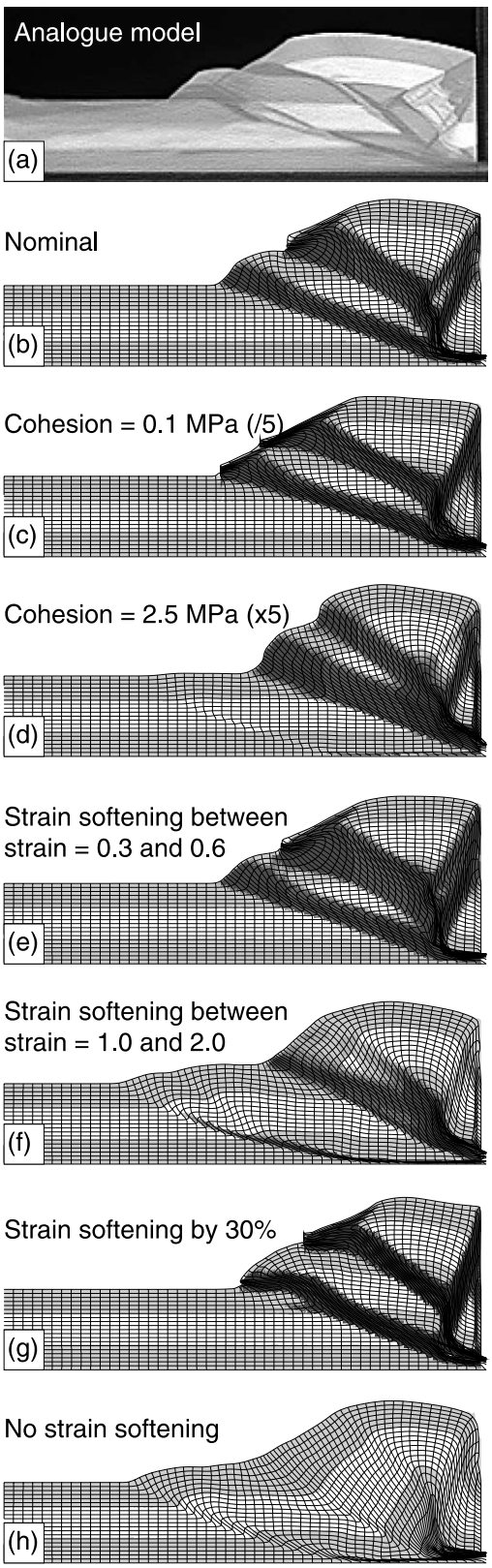

Fig. 10. Sensitivity analyses for the numerical frictional experiment. Frames (b)–(h) are shown after 8 km convergence. (a) Analogue model after 8 cm convergence for comparison. (b) Model from Fig. 8b with cohesion 0.5 MPa, strain-softening threshold 0.5–1.0, and strain-softening amount 15%. (c) Cohesion 0.1 MPa. (d) Cohesion 2.5 MPa. (e) Strain-softening thresholds at strain = 0.3–0.6. (f) Strain-softening thresholds at strain = 1–2. (g) Strain-softening amount 30%. (h) No strain-softening.

backthrusts along the first forward thrust, causes bulging and extension in the upper part of the fault-bend fold, where small normal faults form in its outer arc (Fig. 11a: 6 cm).

Along the second frontal ramp another horse is created as a sub-parallel thrust forms in the hanging wall. Advection of viscous material along the frontal ramp is associated with the initiation of a backthrust. In the footwall of this backthrust, another vague thrust is observed (Fig. 11a: 6 cm shortening). This thrust is probably related to a second pop-up structure that would have been triggered by deformation propagating from the wedge against the wall, if the discontinuity presented by the vertical silicone–sand interface had not localised the position of the frontal ramp. As deformation continues, more backthrusts form as more viscous material is advected along the ramp (Fig. 11a: 8–11 cm shortening).

5.2. Numerical comparison

The strain-localised regions are slow to develop in the numerical model (Fig. 11b), taking until 3 km of convergence to be apparent. As for the analogue case, the first plug forms near the wall and roots within the basal linear viscous layer. The dips of the forward and backward shear zones are 37 and 44°, respectively, higher than in the analogue experiment. This is due to the non-associated plastic flow and consequent neglect of dilational effects in the numerical model.

The tracking grid within the viscous substrate shows how displacement is partitioned there in the form of simple shear, and quickly propagates through the viscous layer. The result is a second forward shear zone, which develops after 4–5 km convergence. In an interesting discrepancy compared with the analogue model, the second pop-up structure forms in-board of the viscous layer termination. We speculate that this difference is caused by the steeper dips of shear zones in the numerical model, which changes the ratio between the pop-up surface width and the layer thickness. In analogue experiments that have a slightly greater viscous substrate width, the second pop-up also forms away from the layer termination. Alternatively, triggering of the end of the viscous layer in the analogue experiment may be enhanced by a slight roughness of the surface of the layer. Sensitivity tests show that a small roughness introduced to the surface of the viscous layer in the numerical experiment is enough to trigger the second thrust at the layer termination.

With continued convergence, the first pop-up near the wall is advected over the footwall. Some upwarping of viscous material against the backstop occurs. A small zone of surface extension is seen in the core of the first pop-up, but unlike the analogue case it does not localise into shear bands. At the same time, the second pop-up shears forward to the viscous layer termination (so that results after a convergence of 7 km are very similar to those seen in the equivalent stage of the analogue model). Viscous material is

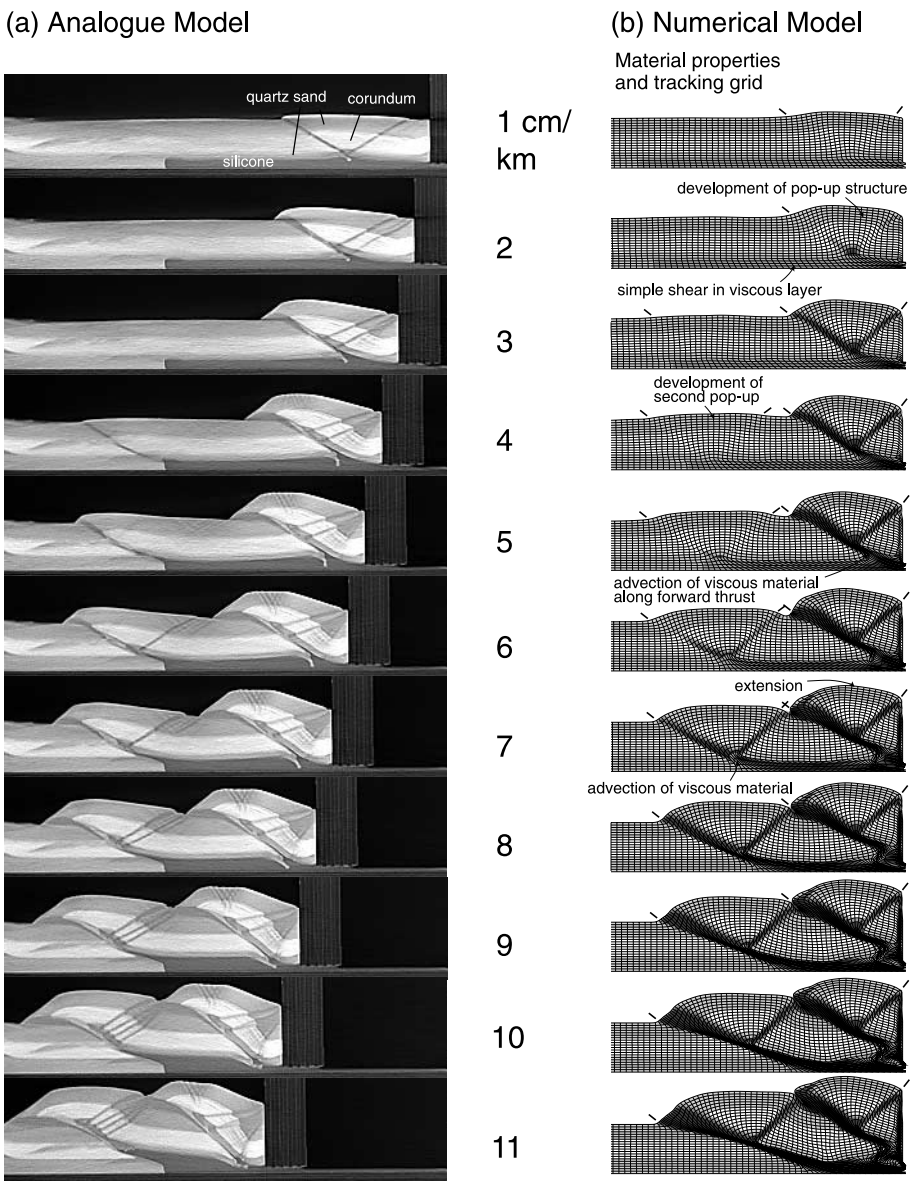

Fig. 11. (a) Results for the analogue frictional-viscous experiment. (b) Equivalent time steps for the numerical model experiment. Cohesion is 0.5 MPa. Frictional strain-softening of 15% between 0.5 and 1.0 of total strain. The small inclined lines at the top of each panel indicate actively deforming shear zones, as determined from strain-rate plots (not shown).

also advected into the core of the second pop-up, causing focusing of the shear zone (cf. the frictional experiment). In comparison with the analogue results, only one backthrust forms as the second pop-up is advected forward. The cause of this difference is unknown, but it may be related to the limited mesh resolution in the numerical model.

5.3. Sensitivity analysis

Fig. 12c shows a frictional-viscous numerical model after 8 km convergence, which is similar to the standard frictional-viscous case from Fig. 11b (reproduced in Fig. 12b) but with increased cohesion. Like results from the equivalent frictional experiment, increased cohesion produces a higher taper of the initial wedge. However, overall the dynamics are not that different from those in Fig. 12b, indicating that cohesion does not exert a first-order control on frictional-viscous behaviour. Fig. 12d and e shows that a much more dramatic change is found for cases with differing basal viscous strength. For a lower viscosity along the basal detachment (Fig. 12d), the second plug at the end of the viscous layer is triggered much earlier, and more deformation occurs along it, with commensurately less deformation and uplift of the initial plug near the wall. In contrast, the case with a higher basal viscosity (Fig. 12e) does not trigger the end of the detachment until ca. 8 km convergence, and instead exhibits a series of forward-stepping thrusts adjacent to the wall, much like the frictional analogue and numerical experiments.

These results show the strong influence of the basal

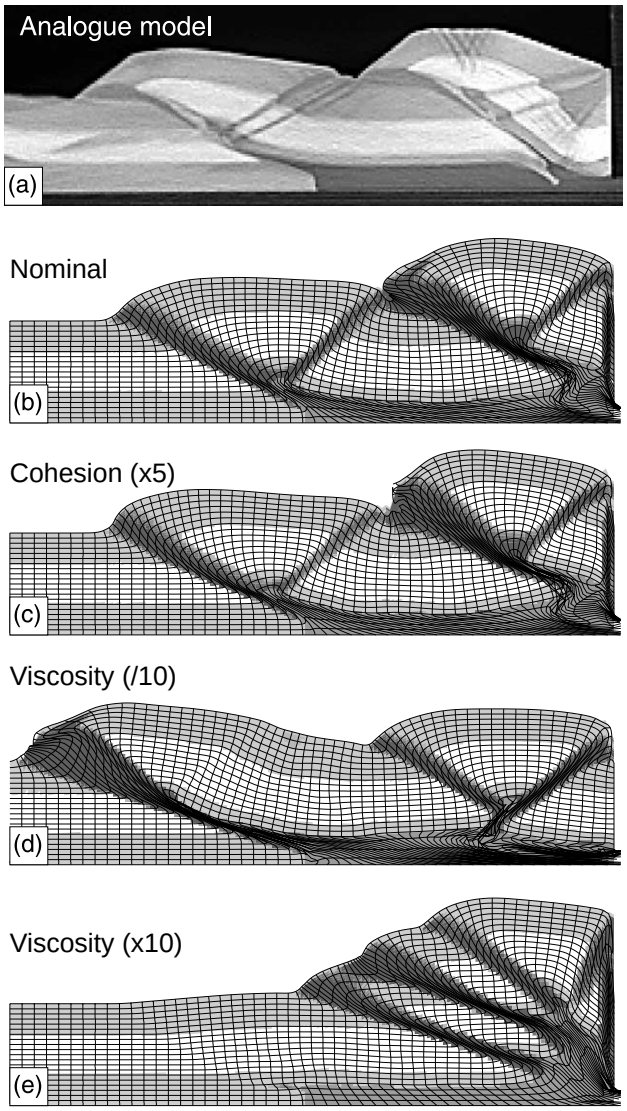

Fig. 12. Sensitivity analyses for the numerical frictional-viscous experiment. Frames (b)–(e) are shown after 8 km convergence. (a) Analogue model after 8 cm convergence. (b) Numerical model from Fig. 11b. (c) Cohesion × 5. (d) Lower viscosity of basal layer. (e) Higher viscosity of basal layer.

detachment on thrust wedge development, consistent with other model studies (e.g. Smart et al., 1999). The dramatic change in dynamics also confirm that our scaling between the analogue and numerical models is basically correct—if it were not, there should be a much bigger discrepancy between the analogue and scaled numerical frictional-viscous models of Fig. 11.

6. Discussion

Very few studies have compared analogue and numerical models results directly. Smart and Couzens-Schultz (2001) compared mechanics of blind thrusting using finite element models and sand/silicone analogue models, but their comparison was limited because of the inability of their numerical model to model shear zones and extreme deformation. The comparison in this paper is more general because the numerical code can incorporate strain-softening and large amounts of deformation, but the numerical code also contains some approximations and simplifications. We discuss some of the effects of these, and the dynamics predicted by the two model types, below.

6.1. In sequence vs. out-of-sequence thrusts

Both analogue and numerical models show fundamental geometric and kinematic differences between frictional and frictional-viscous experiments. The thrust belt that detaches on a frictional décollement (sand) shows a high wedge taper and in-sequence thrusting. The thrust belt advances towards the foreland (away from the mobile wall) by forming new thrust imbricates at the front of the wedge. The older structures within the wedge cease their activity as shortening progresses and are passively transported by displacement on the younger thrusts. The structural vergence of the belt is asymmetric, and is characterized by piggy-back propagation of forward thrusts.

In contrast, the thrust belt that detaches on a weak, viscous décollement (silicone) shows a lower tapered wedge, a more symmetrical vergence of fore- and back-thrusts, and long-lasting coeval activity along different forward thrusts. Previous analogue model experiments simulating detachment on a viscous décollement suggest that there is no systematic forward propagation in a piggy-back fashion and no systematic thrust vergence (Costa and Vendeville, 2002). This behaviour has also been observed in real thrust wedges (e.g. Davis and Engelder, 1985). Our experiments and other similar numerical experiments at basin scale (Wissing et al., 2003) suggest that shortening may be taken up by in-sequence or out-of-sequence thrusting, depending on several factors: (1) the relative strength of the viscous layer, (2) the width and thickness of the viscous layer, (3) the thickness of the overlying frictional layers, and (4) the height of the slot. The numerical experiments also show that the viscous detachment layer deforms by simple shear, whereas the overlying frictional layers deform by localized deformation, resulting in the formation of a pop-up structure during the early stages of shortening.

For low viscosities or large viscous layer thickness, stresses are transmitted easily to the décollement pinch-out. A frontal thrust at the décollement pinch-out nucleates before a second pop-up forms in between frontal thrust and first-formed pop-up, and thrusting is out-of-sequence (Fig. 12d). Conversely, for high viscosities or smaller viscous layer thickness, the stress transfer along the viscous layer is slow. A second pop-up forms within the zone underlain by the viscous layer, before the forward thrust at the

décollement pinch-out is initiated. In this case, thrusting appears to be in-sequence (Fig. 12e).

6.2. Shear zone broadening in the analogue model

After initial strain localisation along relatively narrow shear zones (~1 mm wide), forward shears in the analogue model broaden with increasing convergence. Broadening may occur by a gradual widening in the shear zone (e.g. as seen in the lower part of the frontal thrust in Fig. 8a; 3–4 cm shortening) or by the development of a second semi-parallel discrete thrust in mid-section resulting in a horse structure (e.g. Fig. 8a; 6–7 cm shortening). In both cases deformation occurs dominantly in the hanging wall of the initially narrow forward shear. The formation of horse structures is not seen in the equivalent steps in the numerical model (Fig. 8b), which instead undergoes a progressive broadening of the shear zone with time.

Grain size distributions for quartz and corundum are slightly different, and the dilation between small grains during shearing in the analogue model experiment may potentially influence the strength of the shear zone. In order to test whether grain size heterogeneity had an influence on shear zone broadening, the frictional experiment was repeated, using this time only quartz and corundum sand with a restricted grain size distribution between 125 and 175 μm. Results were almost identical. In yet another experiment, only homogeneous, well-sieved sand (125–175 μm) was used. Again, forward shears broadened during progressive deformation, but horse structures were less clearly defined, suggesting that their development in multi-layer frictional models may be partly controlled by the small change in material properties from quartz sand to corundum sand.

Shear zone broadening in the analogue model by diffuse or discrete deformation appears to be related to one of the two following factors or a combination of them. (1) The initial abrupt transition from lower flat to ramp, which tends to be smoothed out into a more listric fault shape as material is progressively advected along it; this may be accompanied by either an upward migration of diffuse deformation or by the formation of a discrete hanging wall short-cut. (2) The advection of backthrusts—along with material in its footwall—over the ramp of the forward shear. During progressive convergence, backthrusts accommodate less displacement than forward shears. Cessation of activity along a backthrust and its passive transportation along the forward shear may trigger additional diffuse or discrete deformation. Discrete deformation will result in the creation of a horse structure as a new forward shear forms semi-parallel to the older forward shear. The horse structure is accentuated by the fact that the initial forward shear has a slight concave upward shape (which is related to the basal shear stress; cf. Section 6.4), whereas the younger forward shear in its hanging wall tends to be more linear.

The ring shear tests (Section 2.1) indicate that both quartz and corundum sand exhibit elastic/frictional plastic behaviour with strain-hardening prior to failure and subsequent strain-softening until the onset of dynamic stable sliding at constant frictional properties. This behaviour is very similar to experimentally determined stress–strain curves of natural rocks at low confining pressure. Therefore, the results of the analogue model may have implications for the interpretation of natural shear zones in upper crustal rocks. Discrete faults in the model correspond to major through-going fault zones in nature characterized by narrow zones of intense deformation and referred to as fault-cores, whereas diffuse deformation might be expressed in nature by damage zones that occur near major faults and are generally characterized by distributed small-scale faults and fractures (e.g. Chester and Logan, 1986; Chester et al., 1993; Caine et al., 1996; Wilson et al., 2003) Experimental results suggest that: (1) natural shear zones may broaden by diffuse or discrete deformation after initial strain localisation along a narrow fault zone, (2) the width of the shear zone (including associated damage zone) reflects the total cumulative displacement along the fault, (3) deformation tends to become progressively younger in the hanging wall of a forward thrust, and (4) forward shears tend to be broader than back shears (Shipton and Cowie, 2001, 2003).

6.3. Width of shear zones in the numerical model

Since the numerical model uses the continuum approximation, discrete shears cannot be represented The scaled element size was chosen to be smaller than the width of shear zones observed in the analogue model. Some of the shear zones imaged in the numerical model are initially comparable in scaled width to those in the analogue model. The difference occurs when material is advected through shear zones, for example, the forward thrust seen in Fig. 8b. In this case, a ‘numerical diffusion’ occurs between strain-softened and unsoftened regions due to the mesh resolution, causing the strain-softened region to be gradually diffused in the direction of forward propagation, and the shear zone to widen before it is abandoned to form the next (in sequence) thrust. This phenomenon makes it impossible to observe detailed shear zone features, such as the horse structures that develop in the analogue model.

To test the effect of mesh density on numerical model results, the frictional model from Fig. 8b was run at double horizontal mesh density (Fig. 13). Results are shown for 8, 9 and 10 km convergence, and illustrate the same basic dynamics, although some details of the shear zones are different. In particular, the higher mesh density model develops a double shear zone in the second forward-stepping thrust. This is similar to the horse structures seen in the analogue model, and suggests that limited mesh resolution may be misrepresenting these features as one broad shear zone. Despite this difference, the overall similarity in dynamics is encouraging.

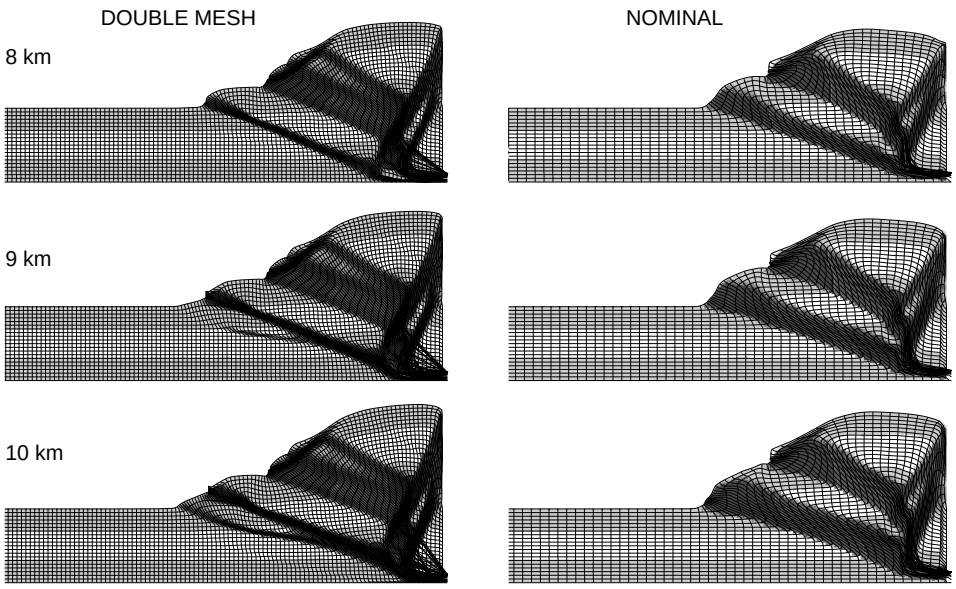

Fig. 13. Effect of increased mesh density on the frictional numerical experiment. Results after 8–10 km convergence with double horizontal mesh density (left-hand side) and results from Fig. 8b (right-hand side) for comparison.

The higher mesh density (Fig. 13a) does not produce narrower shear zones in general, suggesting that these are a function of other parameters. For example, broadening of shear zones in the numerical model may be a function of our choice of strain-softening parameters. In general, the width of thrust slices depends on how long shear can continue to operate on the previous thrust (i.e. how misaligned it can be before a new thrust develops). The sensitivity studies in Section 4.3 illustrated how this depends on the strain-softening parameters. A more realistic material representation of the processes occurring in a shear zone is needed to further explore this effect. This will require more detailed analogue studies to fully constrain the properties of frictional materials.

6.4. Listricity and dip of shear zones

Both the analogue and numerical frictional models show a zone originating from the slot in which the forward thrust is almost horizontal, and which gradually curves up towards the surface. As discussed in Section 4.2, the listricity results from the interaction of horizontal compressive stresses caused by the wall boundary condition, with shear stress along the high-friction base. The basal shear stress causes a rotation in the direction of maximum compressive stress, σ_1 (Mandl, 1988; Mäkel and Walters, 1993). The distance over which the forward shear zone is almost horizontal grows with each episodic thrust slice (Fig. 8a and b). By the development of the third forward thrust, this zone extends under most of the existing wedge.

An important discrepancy between the analogue and numerical models is that the non-associated plastic flow law in the finite element code does not permit dilation. Although the effects on volumetric strain are expected to be small, neglect of dilation means that shear zones that develop in the numerical model are (in general) steeper than the equivalent faults in the analogue model. This is important because it controls the width over which pop-ups develop, and may change the relative timing and sequence of thrusting in frictional and frictional-viscous experiments. The discrepancy in thrust dips may explain why we need cohesion to be at the low end of those scaled from the analogue experiments, in order to reproduce the thrust sequencing seen in Fig. 8a. It may also explain the difference in initial location of the second pop-up (near the décollement termination) between the frictional-viscous analogue and numerical experiments, as shown in Fig. 11. When using this type of numerical model to analyse timing of thrust development and wedge taper in real thrust wedges (e.g. Willett, 1992; Willett et al., 1993), this discrepancy should be taken into account.

7. Concluding remarks

The qualitative agreement between analogue and numerical experiments of frictional and frictional-viscous wedges is encouraging even though discrepancies do exist. It demonstrates that the continuum approximation used in these types of numerical models need not preclude the modelling of frictional materials such as sand, provided caution is taken to properly scale the experiments, and some of the limitations (e.g. in representing dilational and strain-softening parameters) are taken into account. In general, the boundary conditions in nature (for example, those that can generate an accretionary wedge) are not known with certainty as in the laboratory boundary conditions used here. On the other hand, the ‘strong’ boundary condition

imposed at the slot in the experiments shown here provides a relatively stringent test because of the high stresses and strain-rates around this region. The closer match between frictional-viscous analogue and numerical experiments results from a softening of this strong boundary constraint via the viscous medium.

Acknowledgements

Financial support from the Swiss National Science Foundation Grant 2000-0554.11 98/1 and 2000-067952.02, the Hochschulstiftung Bern, and the New Zealand Foundation for Research, Science and Technology is gratefully acknowledged. Jo Lohrmann, Nina Kukowski and Onno Oncken are thanked for providing the opportunity to use the ring shear tester at the GeoForschungsZentrum in Potsdam and for assistance during measurements. We thank Chris Beaumont and the Dalhousie Geodynamics Group for continued access to the numerical code and for useful discussions. Jürgen Adam provided stimulating discussions, and Jo Lohrmann, Susanne Buiter, Laura Wallace and Stuart Read reviewed an earlier version of this paper. We thank reviewers Genene Mulugeta and Kevin Smart for their constructive comments.

References

Abaqus, 2001. Standard, User's Manual, vols. 1 and 2, version 6.2. Abaqus Inc., Pawtucket, RI, USA.

Barnhoorn, A., Bystricky, M., Burlini, L., Kunze, K., 2004. The role of recrystallization on the deformation behaviour of calcite rocks: high strain torsion experiments on Carrara marble. Journal of Structural Geology 26, 885–903.

Barnichon, J.D., Charlier, R., 1996. Finite element modelling of the competition between shear bands in the early stages of thrusting: strain localization analysis and constitutive law influence. In: Buchanan, P.G., Nieuwland, D.A. (Eds.), Modern Developments in Structural Interpretation, Validation and Modelling, Geological Society Special Publication, 99, pp. 235–250.

Beaumont, C., Quinlan, G., 1994. A geodynamic framework for interpreting crustal-scale seismic-reflective patterns in compressional orogens. Geophysical Journal International 116, 754–783.

de Borst, R., 1991. Numerical modelling of bifurcation and localisation in cohesive-frictional materials. Pageoph 137, 367–390.

Byerlee, J.D., 1978. Friction of rocks. Pure Applied Geophysics 116, 615–626.

Caine, J.S., Evans, J.P., Forster, C.B., 1996. Fault zone architecture and permeability structure. Geology 24, 1025–1028.

Calassou, S., Laroque, C., Malavieille, J., 1993. Transfer zones of deformation in thrust wedges: an experimental study. Tectonophysics 221, 325–344.

Chester, F.M., Logan, J.M., 1986. Composite planar fabric of gouge from the Punchbowl Fault, California. Journal of Structural Geology 9, 621–634.

Chester, F.M., Evans, J.P., Biegel, R.L., 1993. Internal structure and weakening mechanisms of the San Andreas fault. Journal of Geophysical Research 98, 771–786.

Colletta, B., Bale, P., Ballard, J.F., Letouzey, J., Pinedo, R., 1991. Computerized X-ray tomography analysis of sandbox models: examples of thin-skinned thrust systems. Geology 19, 1063–1067.

Costa, E., Vendeville, B.C., 2002. Experimental insights on the geometry and kinematics of fold-and-thrust belts above weak, viscous evaporitic décollement. Journal of Structural Geology 24, 1729–1739.

Davis, D.M., Engelder, T., 1985. The role of salt in fold-and-thrust belts. Tectonophysics 119, 67–88.

Davis, D., Suppe, J., Dahlen, F.A., 1983. Mechanics of fold-and-thrust belts and accretionary wedges. Journal of Geophysical Research 88, 1153–1172.

Erickson, S.G., Strayer, L.M., Suppe, J., 2001. Initiation and reactivation of faults during movements over a thrust-fault ramp: numerical mechanical models. Journal of Structural Geology 23, 11–23.

Fullsack, P., 1995. An arbitrary Lagrangian–Eulerian formulation for creeping flows and applications in tectonic models. Geophysical Journal International 120, 1–23.

Gerbault, M., Poliakov, A.N.B., Daignieres, M., 1998. Prediction of faulting from the theories of elasticity and plasticity: what are the limits? Journal of Structural Geology 20, 301–320.

Gutscher, M.A., Kukowski, N., Malavieille, J., Lallemand, S., 1996. Cyclical behavior of thrust wedges; insights from high basal friction sandbox experiments. Geology 24, 135–138.

Gutscher, M.A., Kukowski, N., Malavieille, J., Lallemand, S., 1998. Material transfer in accretionary wedges from analysis of a systematic series of analog experiments. Journal of Structural Geology 20, 407–416.

Hubbert, M.K., 1937. Theory of scale models as applied to the study of geologic structures. Geological Society of America Bulletin 48, 1459–1520.

Huhn, K., 2002. Analyse der Mechanik des Makran Akkretionskeils mit Hilfe der Finiten und der Diskreten elemente Methode sowie analoger Sandexperimente. PhD Thesis, GeoForschungsZentrum Potsdam, Scientific Technical Report STR02/02.

Lallemand, S.E., Schnuerle, P., Malavieille, J., 1994. Coulomb theory applied to accretionary and nonaccretionary wedges; possible causes for tectonic erosion and/or frontal accretion. Journal of Geophysical Research 99, 12033–12055.

Liu, H., McClay, K.R., Powell, D., 1992. Physical models of thrust wedges. In: McClay, K.R., (Ed.), Thrust Tectonics, Chapman and Hall, London, pp. 71–81.

Lohrmann, J., Kukowski, N., Adam, J., Oncken, O., 2003. The impact of analogue material properties on the geometry, kinematics, and dynamics of convergent sand wedges. Journal of Structural Geology 25, 1691–1711.

Mäkel, G., Walters, J., 1993. Finite-element analyses of thrust tectonics: computer simulation of detachment phase and development of thrust faults. Tectonophysics 226, 167–185.

Malavieille, J., 1984. Modélisation expérimentale des chevauchements imbriqués: application aux chaînes des montagnes. Bulletin de la Societé Géologique de France 26, 129–138.

Mandl, G., 1988. Mechanics of Tectonic Faulting: Models and Basic Concepts, Elsevier, Amsterdam.

Mulugeta, G., 1988. Modelling the geometry of Coulomb thrust wedges. Journal of Structural Geology 10, 847–859.

Mulugeta, G., Koyi, H., 1992. Episodic accretion and strain partitioning in a model sand wedge. Tectonophysics 202, 319–333.

Nieuwland, D.A., Leutscher, J.H., Gast, J., 2000. Wedge equilibrium in fold-and-thrust belts: prediction of out-of-sequence thrusting based on sandbox experiments and natural examples. Geologie en Mijnbouw/Netherlands Journal of Geosciences 79, 81–91.

Nino, F., Philip, H., Chery, J., 1998. The role of bed-parallel slip in the formation of blind thrust faults. Journal of Structural Geology 20, 503–516.

Philippe, Y., 1994. Transfer zone in the southern Jura thrust belt (eastern France): geometry, development and comparison with analogue modelling experiments. In: Mascle, A., (Ed.), Hydrocarbon and

Petroleum Geology of France, European Association of Petroleum Geologists, 4., pp. 327–346.

Ramberg, H., 1981. Gravity, Deformation and the Earth's Crust, Academic Press, New York.

Ramsay, J.G., Graham, R.H., 1970. Strain variations in shear belts. Canadian Journal of Earth Sciences 7, 786–813.

Sassi, W., Faure, J.-L., 1997. Role of faults and layer interfaces on the spatial variation of stress regimes in basins: inferences from numerical modelling. Tectonophysics 266, 101–119.

Sassi, W., Colletta, B., Balé, P., Paquereau, T., 1993. Modelling of structural complexity in sedimentary basins. Tectonophysics 226, 97–112.

Schellart, W.P., 2000. Shear test results for cohesion and friction coefficients for different granular materials: scaling implications for their usage in analogue modelling. Tectonophysics 324, 1–16.

Schreurs, G., Hänni, R., Vock, P., 2001. Four-dimensional analysis of analog models: experiments on transfer zones in fold and thrust belts. In: Koyi, H.A., Mancktelow, N. (Eds.), Tectonic Modeling: A Volume in Honor of Hans Ramberg, Geological Society of America Memoir, 193., pp. 179–190.

Schulze, D., 1994. Entwicklung und Anwendung eines neuartigen Ringschergerätes. Aufbereitungs-Technik 35, 524–535.

Shipton, Z.K., Cowie, P.A., 2001. Damage zone and slip-surface evolution over μm to km scales in high-porosity Navajo sandstone, Utah. Journal of Structural Geology 23, 1825–1844.

Shipton, Z.K., Cowie, P.A., 2003. A conceptual model for the origin of fault damage zone structures in high-porosity sandstone. Journal of Structural Geology 24, 333–344.

Smart, K.J., Couzens-Schultz, B.A., 2001. Mechanics of blind thrusting: comparison of numerical and physical modeling. Journal of Geology 109, 771–779.

Smart, K.J., Krieg, R.D., Dunne, W.M., 1999. Deformation behavior during blind thrust translation as a function of fault strength. Journal of Structural Geology 21, 855–874.

Storti, F., Salvini, F., McClay, K., 1997. Fault-related folding in sandbox analogue models of thrust wedges. Journal of Structural Geology 19, 583–602.

Strayer, L.M., Hudleston, P.J., Lorig, L.J., 2001. A numerical model of deformation and fluid-flow in an evolving thrust wedge. Tectonophysics 335, 121–145.

Upton, P., 1998. Modelling localization of deformation and fluid flow in a compressional orogen; implications for the Southern Alps of New Zealand. American Journal of Science 4, 296–323.

Vanbrabant, Y., Jongmans, D., Hassani, R., Bellino, D., 1999. An application of two-dimensional finite-element modelling for studying the deformation of the Variscan fold-and-thrust belt (Belgium). Tectonophysics 309, 141–159.

Vendeville, B.C., Cobbold, P.R., Davy, P., Brun, J.P., Choukroune, P., 1987. Physical models of extensional tectonics at various scales. In: Coward, M.P., Dewey, J.F., Hancock, P.L. (Eds.), Continental Extensional Tectonics, Geological Society of London Special Publication, 28., pp. 95–107.

Vermeer, P.A., de Borst, R., 1984. Non-associated plasticity for soils, concrete and rock. Heron 29, 1–62.

Weijermars, R., 1986. Flow behaviour and physical chemistry of bouncing putties and related polymers in view of tectonic laboratory applications. Tectonophysics 124, 325–358.

Willett, S.D., 1992. Dynamic and kinematic growth and change of a Coulomb wedge. In: McClay, K.R., (Ed.), Thrust Tectonics, Chapman and Hall, London, pp. 19–31.

Willett, S., Beaumont, C., Fullsack, P., 1993. A mechanical model for the tectonics of doubly vergent compressional orogens. Geology 21, 371–374.

Wilson, J.E., Chester, J.S., Chester, F.M., 2003. Microfracture analysis of fault growth and wear processes, Punchbowl Fault, San Andreas system, California. Journal of Structural Geology 25, 1855–1873.

Wissing, S., Ellis, S., Pfiffner, O.A., 2003. Numerical models of Alpine-type cover nappes. Tectonophysics 367, 145–172.

Zienkiewicz, O.C., Humpheson, C., Lewis, R.W., 1975. Associated and non-associated visco-plasticity and plasticity in soil mechanics. Géotechnique 25, 671–689.